nature nanotechnology

Article

https://doi.org/10.1038/s41565-024-01746-7

Coupled nanopores for single-molecule detection

Received: 25 July 2022

Accepted: 5 July 2024

Yung-Chien Chou[1,4], **Chih-Yuan Lin**[1,4], **Alice Castan**[1], **Joshua Chen**[1], **Rachael Keneipp**[1], **Parisa Yasini**[1], **Dimitri Monos**[2,3] & **Marija Drndić**[1] ✉

Rapid sensing of molecules is increasingly important in many studies and applications, such as DNA sequencing and protein identification. Here, beyond atomically thin 2D nanopores, we conceptualize, simulate and experimentally demonstrate coupled, guiding and reusable bilayer nanopore platforms, enabling advanced ultrafast detection of unmodified molecules. The bottom layer can collimate and decelerate the molecule before it enters the sensing zone, and the top 2D pore (~2 nm) enables position sensing. We varied the number of pores in the bottom layer from one to nine while fixing one 2D pore in the top layer. When the number of pores in the bottom layer is reduced to one, sensing is performed by both layers, and distinct T- and W-shaped translocation signals indicate the precise position of molecules and are sensitive to fragment lengths. This is uniquely enabled by microsecond resolution capabilities and precision nanofabrication. Coupled nanopores represent configurable multifunctional systems with inter- and intralayer structures for improved electromechanical control and prolonged dwell times in a 2D sensing zone.

Detecting single molecules with electrical and optical approaches has advanced understanding of fundamental processes and the correlation of structure and properties at the single-particle level[1]. The idea of counting particles through holes evolved into resistive-pulse sensing, where molecules produce current blockades, allowing enzyme-assisted DNA sequencing[2], biomarker detection and usage in filtration and desalination[3–7]. Labelling molecules with markers such as nanoparticles and attaching them to carriers, such as double-stranded DNA (dsDNA), have been some of the proxy approaches to increase sensitivity[8] while reducing the need for small pores. These approaches require sample modification, which often alters interactions and dynamics. Alternatively, or in addition, designing internal pore layers and scaling pores down to atomic scale while simultaneously improving signal-to-noise ratio and time resolution can enable direct and ultrafast reading of unmodified molecules and their dynamics[9,10] at unprecedented resolution. At typical translocation rates of 0.1–1 μs bp^{-1} (ref. 9), DNA travels a 10 nm distance in ~3–30 μs, which is within the experimental resolution reach. Integrating guiding structures at this scale into pores can facilitate local velocity control of translocating molecules.

In this Article, we introduce a bilayer-coupled nanopore concept for ultrafast guiding, tracking and detecting single unmodified molecules (as illustrated in Fig. 1a). Conceptually, coupled nanopores can be treated as one complex nanopore with a modular internal structure. This differs from double-pore devices where pores were positioned in parallel to control the motion of molecules and enhance signal reading[11–14]. The fabrication dimensions in this work are down to several nanometres, representing a significant advancement over previous two-pore devices where pores were positioned in series[15–17]. Our pore separations are about 100 times smaller, and pore diameters are over 10 times smaller (Extended Data Table 1). Previous designs with large pore separation allowed DNA to recoil between pores instead of occupying two pores simultaneously[16]. These substantially larger cavities were utilized to trap and recapture long DNA molecules[15,17] or perform time-of-flight measurements[16]. The creation of pores at distances comparable to the persistence

---

[1]Department of Physics and Astronomy, University of Pennsylvania, Philadelphia, PA, USA. [2]Department of Pathology and Laboratory Medicine, Perelman School of Medicine, University of Pennsylvania, Philadelphia, PA, USA. [3]Department of Pathology and Laboratory Medicine, Children's Hospital of Philadelphia, Philadelphia, PA, USA. [4]These authors contributed equally: Yung-Chien Chou, Chih-Yuan Lin. ✉e-mail: drndic@sas.upenn.edu

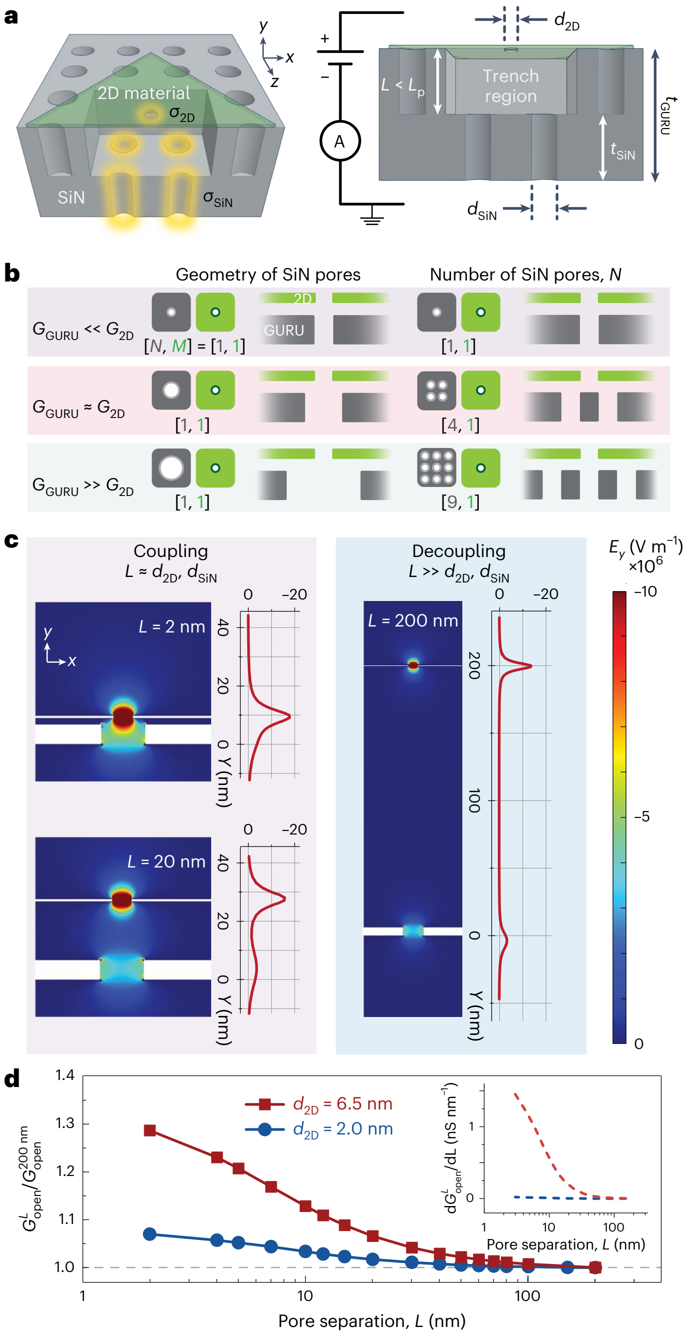

Fig. 1 | Coupled bilayer nanopore concept for physical guiding, tracking and sizing of single molecules. **a**, Fabrication schematic including EBL, etching, 2D materials transfer and AC-STEM sculpting. SiN nanopores constitute a GURU platform. Pore thicknesses are t_{SiN} and t_{2D}, diameters are d_{SiN} and d_{2D} and the total thickness is t_{GURU}. Device configurations are denoted as $[N, M]$ for N SiN pores and M 2D pores. σ_{SiN} and σ_{2D} denote surface charge densities of SiN and 2D pores, respectively. The interlayer separation, L, can be experimentally controlled by the duration of RIE. **b**, Conductance regimes and $[N, 1]$ configurations: $G_{\mathrm{GURU}} \ll G_{\mathrm{2D}}$, $G_{\mathrm{GURU}} \approx G_{\mathrm{2D}}$ and $G_{\mathrm{GURU}} \gg G_{\mathrm{2D}}$. G_{GURU} and G_{2D} are the conductance of the SiN ('GURU') and 2D layers, respectively. **c**, Electric field profiles for [1, 1]. $d_{\mathrm{2D}} = 6.5$ nm, $d_{\mathrm{SiN}} = 15$ nm, $t_{\mathrm{2D}} = 1$ nm, $t_{\mathrm{SiN}} = 7$ nm. $L = 2$, 20 nm (coupling) and 200 nm (decoupling regime). **d**, Conductance ratio of $G(L)/G(L = 200\ \mathrm{nm})$ and $\Delta G/\Delta L$ for [1, 1] versus L; the slope $\Delta G/\Delta L \approx 1$ nS nm^{-1} for $L \approx 10$ nm.

length represents an entirely new regime of transport phenomena. Additionally, small pore diameters in our work introduce stronger electric fields. Consequently, this degree of spatial confinement enhances nanopore coupling.

Device design and fabrication

The device consists of two layers with configurable structures at nanometre precision: a top two-dimensional (2D) material flake with a single pore, and a bottom silicon nitride (SiN) layer containing one or more pores in the bottom layer (Fig. 1a). The schematic on the right shows the cross-section of the two-layered device defining the relevant dimensions (L, L_{p}, d_{2D}, d_{SiN}, t_{SiN} and t_{GURU}) with the corresponding three-dimensional simulation detailed in Supplementary Fig. 1. The SiN trench is shown, and the nanopores used for ion transport are highlighted. Device configurations are labelled as $[N, M]$ for N SiN pores and M 2D pores.

One or more pores can be placed within each layer, and pore conductance is tailored via their geometry and charge. Different sensor regimes are theoretically possible by varying the number of pores in the bottom layer from several to one, while restricting the number in the top layer to one 2D pore. When interlayer separation, L, is comparable to or smaller than the persistence length of polymers, L_{p} (for example, dsDNA), the polymer behaves locally like a rigid rod. This flexible design of the coupled nanopores where $L < L_{\mathrm{p}}$ provides capabilities to constrain polymers before entering the final sensing layer. Being unique components for atom-scale engineering, 2D materials are optimal for achieving high spatial resolution[18] and stackable modularity[19] for the bilayer-coupled nanopore design.

Here, we position a 2D monolayer above 'guiding and reusable' ('GURU') SiN layer that can be as thin as 1 nm (refs. 20,21). Geometric parameters are experimentally controlled with nanometre precision using lithography, etching, sculpting[22–24] and surface charges via material choice. For brevity, we refer to the two layers as the 'GURU layer' and the '2D layer', and the devices as '2D-GURU'.

Coupling of electric fields

Figure 1b shows the various conductance regimes and device configurations including $G_{\mathrm{GURU}} \ll G_{\mathrm{2D}}$, $G_{\mathrm{GURU}} \approx G_{\mathrm{2D}}$ and $G_{\mathrm{GURU}} \gg G_{\mathrm{2D}}$, where G_{GURU} and G_{2D} are the conductance of the GURU and 2D layers, respectively. For example, when the 2D layer has a fixed geometry, the regime of comparable layer conductances, $G_{\mathrm{2D}} \approx G_{\mathrm{GURU}}$, can be reached by varying N or d_{SiN} (Supplementary Fig. 2).

When two pores are in close vicinity (the layer separation $L \approx d_{\mathrm{2D}}, d_{\mathrm{SiN}}$), their electric fields overlap (Fig. 1c). The coupling effect requires two crucial elements: (1) layer separation and (2) pore diameters. If the two pores are positioned far from each other ($L \gg d_{\mathrm{2D}}, d_{\mathrm{SiN}}$), electric fields remain independent and decoupled (illustrated in Fig. 1c for $L = 200$ nm).

For two stacked nanometre-diameter pores, the coupling effects can be examined by conductance ratios ($G^{L}_{\mathrm{open}}/G^{200\mathrm{nm}}_{\mathrm{open}}$) with interlayer separation L (Fig. 1d). As L decreases, conductance ratios increase and exceed unity, marking a departure from decoupled to coupled pores. In other words, the equivalent resistance of two coupled pores in series is smaller than the sum of individual pore resistances.

Nanopore coupling also gives rise to a non-zero rate of change of conductance with decreasing interlayer separation L (Fig. 1d). For example, $\Delta G/\Delta L$ is ~1 nS nm^{-1} at $L \approx 10$ nm (for $d_{\mathrm{2D}}/d_{\mathrm{SiN}} = 6.5\ \mathrm{nm}/15.0\ \mathrm{nm} = 0.43$). G is sensitive to nanometre-size changes in L, presenting a new strategy to exploit nanopore coupling to probe subnanometre membrane vibrations and distances electrically.

GURU nanopore systems

GURU layers are configurable through a fabrication process that includes electron beam lithography (EBL), reactive ion etching (RIE) and transmission electron microscopy (TEM). This is illustrated in Extended Data Fig. 1, with the resulting TEM images shown in Fig. 2a. GURU platforms are reusable, as exemplified by [9, 1], where Chip D was reused four times (four cycles of 2D material transfer and eight cycles of piranha surface treatment) (also see Supplementary Section 3). The 2D pores were drilled by aberration-corrected scanning

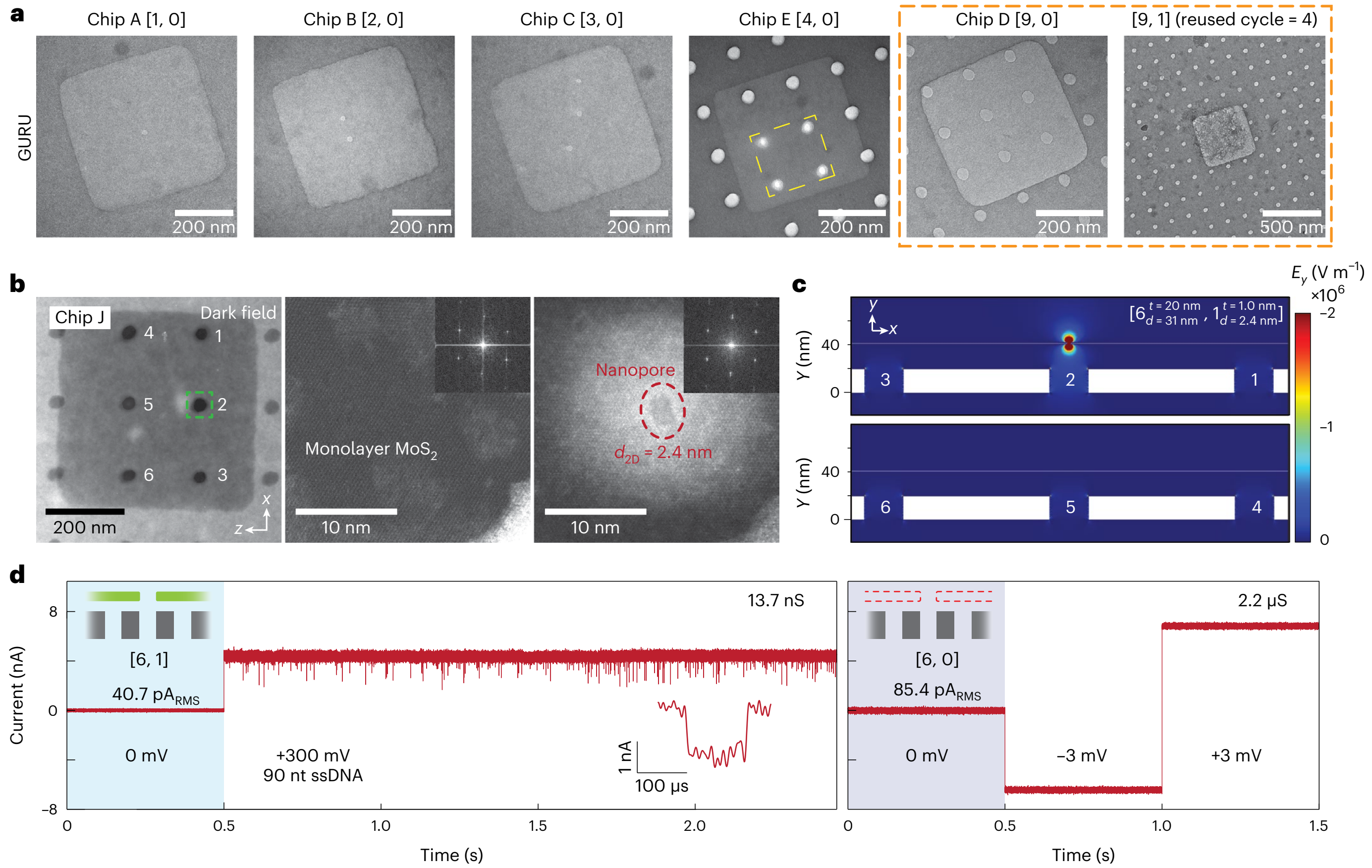

Fig. 2 | [*N*, 1] configurations: TEM images, modelling and measurements. **a**, Bright-field (BF) TEM images of GURU layers: $L = 20 \pm 1$ nm for [1, 0] to [3, 0] and [9, 0], $L = 100 \pm 1$ nm for [4, 0]. Nanopores in the GURU layers are made with TEM drilling (Chip A [1, 0], Chip B [2, 0], Chip C [3, 0]), EBL/RIE (Chip D [9, 0]) and a combination of both for Chip E [4, 0] that contained a thicker SiN membrane. The dashed yellow square in the Chip E [4, 0] configuration indicates where TEM drilling is used, while the other pore-looking regions in this device were made by EBL and RIE but were not etched all the way through. The TEM drilling was then used to drill through the four locations. From left to right the device parameters are [t_{GURU} (nm), trench depth (nm))] = [40, 20], [40, 20], [40, 20], [130, 20], [40, 20], [40, 20]. Image of [9, 1] after reusing it for four times (orange rectangle). **b**, Dark-field (DF) AC-STEM images (*xz* plane) of Chip J, [6, 1], with a monolayer (2D) MoS_2 nanopore, d_{2D} (TEM) = 2.4 ± 0.5 nm (red oval). Diameter errors are included from TEM images and reflect the as-fabricated pores. Images are focused on the bottom of the SiN layer. Insets are fast Fourier transforms (FFTs) of the hexagonal 2D lattice before and after pore formation. The 2D pore is drilled below pore 2 (light-green square). **c**, Simulated electric field profiles of [6, 1] in *xy* planes containing pores 1–3 and 4–6, respectively. Geometric parameters are indicated, and $L = 20$ nm. **d**, Data from Chip J with 90 nt ssDNA. Current–time trace at 300 mV and 1 M KCl, recorded at 1 MHz bandwidth and Bessel filtered at 100 kHz. A 3-s-long current–time trace is displayed from a 70 min experiment. $G = 13.7$ nS. $L = 20 \pm 1$ nm, $t_{\mathrm{GURU}} = 40 \pm 3$ nm and d_{SiN} (TEM) = 31.0 ± 0.9 nm. For [6, 0], $G_{\mathrm{GURU}} = 2.2$ μS » G_{2D}. I_{rms} at 0 V is shown for [6, 1] and [6, 0]. Diameter errors are included from TEM images and reflect the as-fabricated pores. See Methods for diameter and error analysis.

transmission electron microscopy (AC-STEM) in all cases, and the small diameters d_{2D} were designed for dsDNA to pass unfolded. The gradual subnanometre drilling process is shown in Extended Data Figs. 2–4. Successful storage, wetting and low-noise stable performance were developed in this work (Methods). Wafer-scale integration is viable with multiple trench patterning (Extended Data Fig. 5a) and proper nanofluidic design. Some samples used for ionic testing were coated with a thin layer of HfO_2 for additional robustness and to tailor pore sizes (Extended Data Fig. 5b). The nanopore coupling is not affected by choice of fabrication methods (EBL, RIE or TEM) but rather by device dimensions.

In the bottom layer, the number of SiN pores $N > 1$, can be optimized for molecule guiding, while the top 2D pore enables primary sensing. DNA pre-confinement was previously shown using a nanoporous filtering membrane with ~50-nm-diameter pores placed at an order of magnitude larger distance ($L \approx 200$ nm) from a 6.7–8.0-nm-diameter SiN pore, reporting a suppressed frequency of folded DNA translocations[25]. Other efforts on large filtering arrays ($N > 100$) could not demonstrate translocations due to device failure modes[10].

The GURU layer resistance in Fig. 2b was designed to be negligible ($G_{\mathrm{2D}} \ll G_{\mathrm{GURU}}$). The open-pore conductance $G \approx G_{\mathrm{2D}}$ was 13.7 nS in 1 M KCl, in agreement with the calculated value assuming $t_{\mathrm{2D}} = 2.2 \pm 1.2$ nm, where the error in t_{2D} is calculated from the error in TEM-estimated diameter (Methods). The coupled electric field profiles (Fig. 2c) are mapped accordingly. Figure 2d demonstrates the detection of 90-nucleotide (nt) single-stranded DNA (ssDNA) with this [6, 1] (Chip J) device. Another dataset with [4, 1] (Chip K) is shown in Supplementary Fig. 3. A detailed analysis of translocation dynamics is shown in Supplementary Figs. 4–6, including the exponentially fitted distribution of dwell times for various voltages. The observed longer translocation time per nanometre, compared with the previous study with a 2D MoS_2 nanopore[26] (Supplementary Section 5), indicates that the GURU layer can prolong the translocation time in the desired sensing zone.

The 2D flake was annealed to the SiN layer, and the suspended area of the 2D material was minimized to ensure robustness. A stable ionic current was observed. When the 2D material was chemically removed (Fig. 2d), the conductance increased substantially, G_{GURU}

https://doi.org/10.1038/s41565-024-01746-7

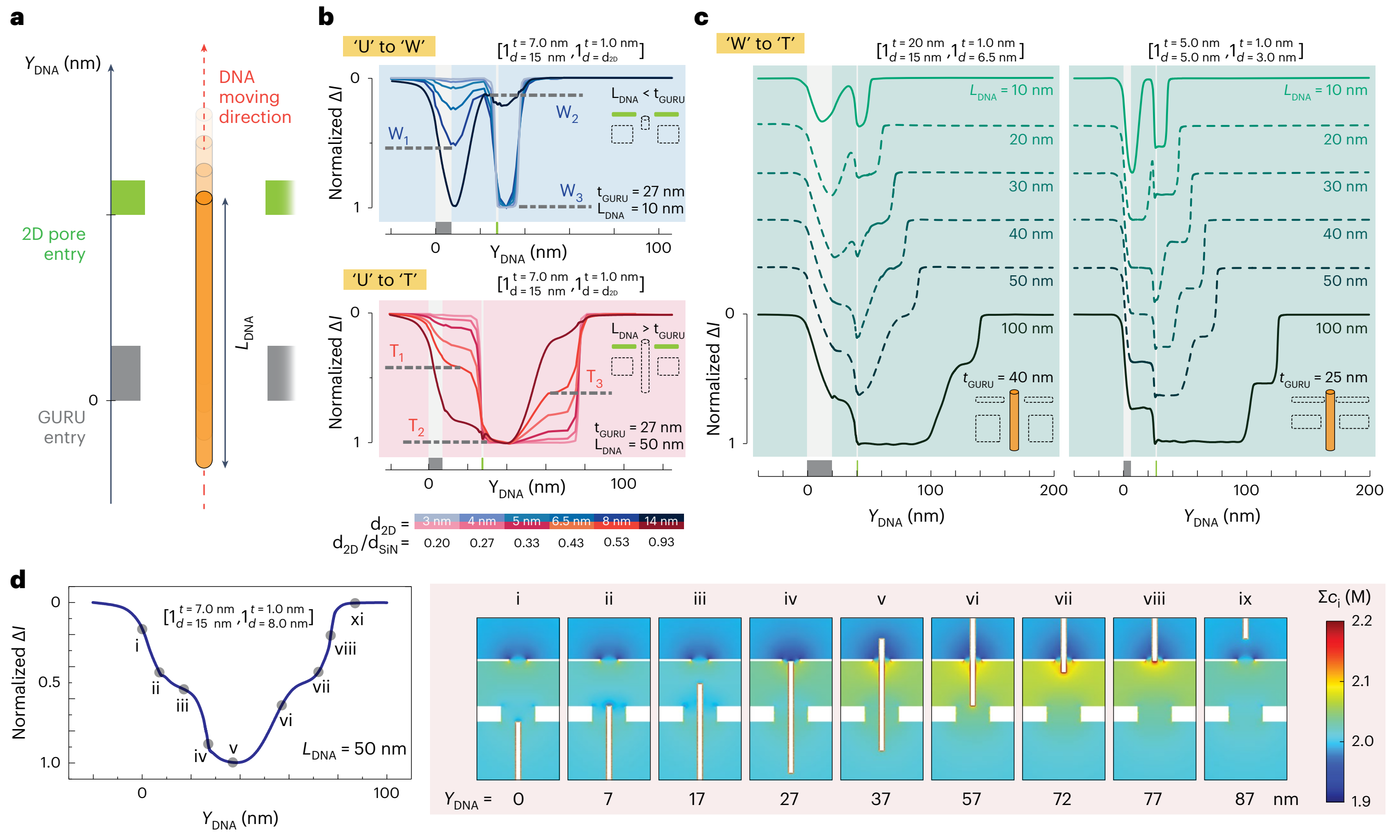

Fig. 3 | Simulations of coupled configuration [1, 1]. **a**, Simulated ionic currents versus dsDNA position along the *y* direction assuming straight trajectories. Simplified schematics are shown. Y_{DNA} is the coordinate of the dsDNA front. dsDNA is simulated as a charged rod entering from the GURU side ($Y_{DNA} = 0$). L_{DNA} is the DNA length. **b**, Evolution from U to W ($L_{DNA} < t_{GURU}$) and from U to T events ($L_{DNA} > t_{GURU}$) for [1, 1] geometry for d_{2D} = 3–14 nm. Pore dimensions and pore *y* positions are indicated, *V* = 200 mV. Maximum intraevent magnitudes are normalized to 1. The solid colour in the schematic marks what is varied. **c**, Evolution from W to T events for L_{DNA} = 10–50 nm (ΔL_{DNA} = 10 nm), and L_{DNA} = 100 nm for [1, 1], *L* = 20 nm. Pore geometries and *y* positions are indicated. *V* = 300 mV (left) and 200 mV (right). Maximum interevent magnitude is normalized to 1 as L_{DNA} = 100 nm ($>t_{GURU}$). **d**, Left: simulated event blockade illustrates an example of symmetric T_1 and T_3 sublevels; configurations are shown as indicated. Right: spatial profiles (*i* to *ix*) of the total concentration, $\sum c_i$, of potassium and chloride ions (Methods) for the corresponding Y_{DNA} as DNA molecule translocates. The maximum event magnitude is normalized to 1.

([6, 0]) = 2.2 µS, matching the calculated value from the sum of six SiN pores (array conductance, G_{GURU}, increases with *N* and d_{SiN} (ref. 10)).

Principle of molecule tracking with coupled pores

Distinctive translocating ionic signal patterns arise due to the coupling of electric fields of nearby nanopores. We performed current simulations in open pores and with dsDNA blockades at varying *y* positions, Y_{DNA}, for different device configurations (Fig. 3a). DNA was modelled as a rigid rod. The details of modelling[14,27] are provided in Supplementary Section 1. For decoupled pores, two events occur independently as the DNA first blocks one and then the other pore. Also, when the SiN layer is much more conductive than the 2D pore ($G_{2D} \ll G_{GURU}$), as in [6, 1] (Fig. 2), typical U events will arise from the DNA blocking the 2D pore. These scenarios are shown in Supplementary Figs. 7–9.

Non-trivial event signals arise when the two nearby layers have comparable conductances, $G_{2D} \approx G_{GURU}$. When we limit the number of pores, *N* and *M*, to one pore in each layer ($N = M = 1$), we observe the interference from both pores and blockade patterns resembling variations of 'W' and 'T' shapes versus dsDNA positions (Fig. 3b,c). As the coupled electric field distributes across the two pores, the blockade in one pore interferes with that in the other. In this simulation, these signal shapes are mostly symmetrical ($T_1 \approx T_3$) when the individual current blockades of dsDNA are similar, which illustrates examples of non-trivial signals arising from the GURU structure. For example, the simulation result demonstrates the influence of voltage on the asymmetry of T_1 and T_3, which can result from the ions depleted zone in front of the DNA when DNA occupies only the SiN pore and the accumulation of ions in the trench region when DNA occupies only the 2D pore (Fig. 3d and Supplementary Fig. 10).

We show theoretically, for d_{2D} = 3 nm to 14 nm, how signals evolve from U to W and U to T-like signals, for L_{DNA} < and > t_{GURU}, respectively, by fixing other parameters. The range of d_{2D}, corresponding to d_{2D}/d_{SiN} = 0.20–0.93, is determined on the basis of the open-pore conductances, and modelling for the data is shown in Fig. 4a. Signal sublevels are marked as $T_{1–3}$ for T events and $W_{1–3}$ for W events. The minimum and maximum blockade sublevels are W_2 (dsDNA in the trench) and T_2 (cross-layer dsDNA occupancy), respectively.

With the coupling effect, T_2 depth is not the sum of T_1 and T_3 (single-layer dsDNA occupancy), and T_1 can be >, ≈, or <T_3 (Fig. 4d, Supplementary Fig. 10 and Supplementary Section 6.3). Figure 3c displays simulated signal shape evolution as L_{DNA} increases by 10 nm for two sets of geometric parameters in [1, 1]. W events occur where $L_{DNA} < t_{GURU}$, while T events emerge where $L_{DNA} > t_{GURU}$. These results indicate signal sensitivity to nanometre-size changes in L_{DNA}, in principle allowing accurate single-molecule fragment sizing. From *G* (at fixed Y_{DNA}) versus L_{DNA} (Supplementary Fig. 11), we estimate the change of conductance per change in DNA fragment length as $\Delta G/\Delta L_{DNA} \approx$ 2–9 nS kbp^{-1}. Moreover, sublevel time stamp analysis would allow real-time label-free DNA position tracking with nanometre accuracy. These theoretical findings (Fig. 3) clearly show the diversity and flexibility of 2D-GURU devices

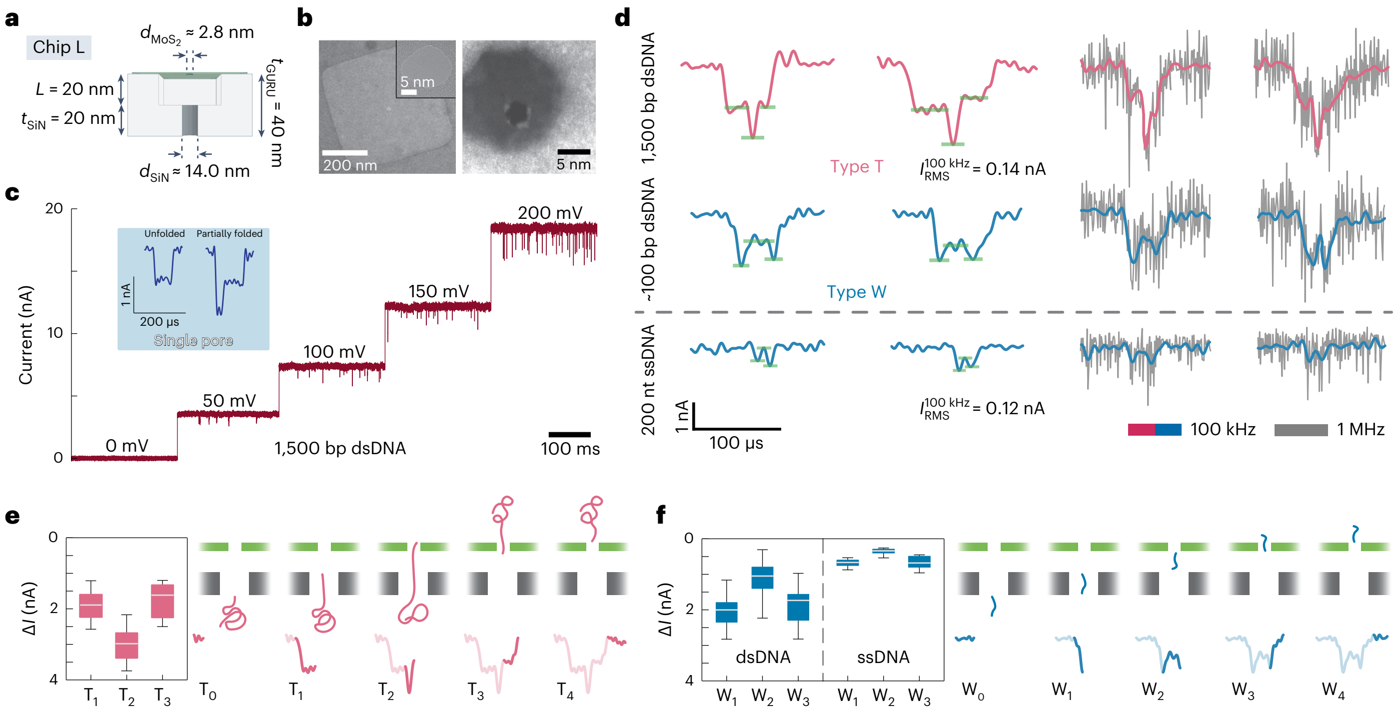

Fig. 4 | Ionic experiments with [1, 1] configuration. a,**b**, Bright-field (BF) and dark-field (DF) TEM/AC-STEM images of [1,1], $G_{2D} \approx G_{GURU}$. The as-fabricated TEM-measured pore diameters for Chip L were d_{2D} (TEM) = 2.8 ± 0.7 nm, d_{SiN} (TEM) = 14.0 ± 0.9 nm, t_{GURU} = 40 ± 3 nm, L = 20 ± 1 nm. Diameter errors are included from TEM images and reflect the as-fabricated pores. **c**, Ionic current versus time for open-pore current at 0 V and after adding 1,500 bp dsDNA at 50, 100, 150 and 200 mV in 1 M KCl. Inset: conventional shapes for unfolded and partially folded DNA translocation events are acquired from a single comparable, small and thin, nanopore. **d**, T and W events. At V = 200 mV, T events for 1,500 bp dsDNA and W events for ~100 bp dsDNA; W events for 200 nt ssDNA. 1 M KCl, 1 MHz bandwidth, Bessel filtered at 100 kHz. **e**,**f**, Schematics illustrating DNA translocations and boxplots of event depths, T_1 to T_3 and W_1 to W_3 for data in **d**. The box ranges from the first to the third interquartile, and the median is indicated by a horizontal line within the box, with whiskers extending to the minimum and maximum values of the dataset. In **e**, n = 61; in **f**, n = 36 for dsDNA and n = 94 for ssDNA.

with [1, 1] configuration in predicting signal evolution across a range of DNA fragment lengths. It also reveals that implementing these theoretical findings would require customizing experimental parameters (for example, L, t_{GURU} and d_{2D}/d_{SiN}) to accommodate DNA lengths.

Experimental demonstration of DNA tracking

To demonstrate position tracking capabilities of couple pores, we measured DNA of different lengths using two-pore devices with [1, 1] geometry, varying pore sizes and separations (Figs. 4 and 5). Measurements were conducted up to 1 MHz bandwidth for Chip L and up to 10 MHz bandwidth for Chips M and N.

Detected current–time traces and event shapes resemble simulations in Fig. 3 and starkly contrast to the typical U-shape events produced by comparable small-diameter single pores (Fig. 4c, inset). These short signal features from label-free DNA passing through two pores are distinguishable at high bandwidth (root-mean-square noise $I_{rms}^{1MHz} \approx 0.5$ nA) because the pores are thin and signal-to-noise ratio high enough. The ultrafast detection comes at the price of sacrificing low-magnitude signals and distorting the distribution towards deeper events, presenting an experimental tug-of-war between low noise and high time resolution. Time resolution is prioritized here to detect DNA passage through both pores. Orders of magnitude faster detection is an advantage over protein pores in applications where minimizing measurement time is non-negligent. The dwell time histogram for various voltages is shown in Supplementary Fig. 5. Furthermore, the mean capture rates for [6, 1] (Chip J) and [1, 1] (Chip L) devices show exponential dependence on applied voltage (Supplementary Fig. 6), suggesting voltage activation in the capture of DNA[28].

For short DNA length, L_{DNA} (200 nt ssDNA), most detected events were W events; T events were extremely rare (<0.6%) (Fig. 4d, bottom). Although short ssDNA could, in principle, stretch across pores ($L_{DNA} \approx 126$ nm > L), this is unlikely since $L_p \approx 1$ nm « L (ref. 29). As expected, W events from ssDNA could still be resolved with a magnitude about half that for dsDNA W events using the same device.

The translocation measurements for 1,500 bp dsDNA ($L_{DNA} \approx 450$ nm) are displayed in Fig. 4c,d. T events are detected as expected for L_{DNA} » t_{GURU} where dsDNA translocates like a rod, with $L_p \approx 35$–50 nm > L (refs. 29,30). Selected long events at 50 mV (Supplementary Fig. 12) show a timescale similar to the polymer relaxation (Zimm) time[31]. Rare W events (~5%) were detected with a shorter dwell time than T events. Similar depths of $W_{1,3} \approx T_{1,3}$ hint at possible fragmented dsDNA degradation. We performed gel electrophoresis on the measured sample (Supplementary Fig. 13). Average sizing signals of ~1,300 bp dsDNA were detected from samples containing 1,500 bp dsDNA, without clear indications of fragmented pieces. Yet, the tool limitation was validated using mixtures of pure samples (1,500 bp and 100 bp dsDNA, 0.5–50%), where the controlled mix of 1% 100 bp dsDNA best-matched electrophoresis signals of the measured sample detecting 'W events'. Our data reveal the unprecedented ability and sensitivity of GURU devices to discriminate low-concentration (<1%) analytes within the same sample. In contrast, a single-pore sensor produces unanimous U events (Fig. 4c, inset) with uniform event depths but wide dwell time distributions[32]. Other factors that may affect event shapes are discussed in Supplementary Section 10 (Supplementary Figs. 14–16).

Figure 4e,f shows the magnitudes of the different current sublevels observed for dsDNA and ssDNA in the same device. Note that

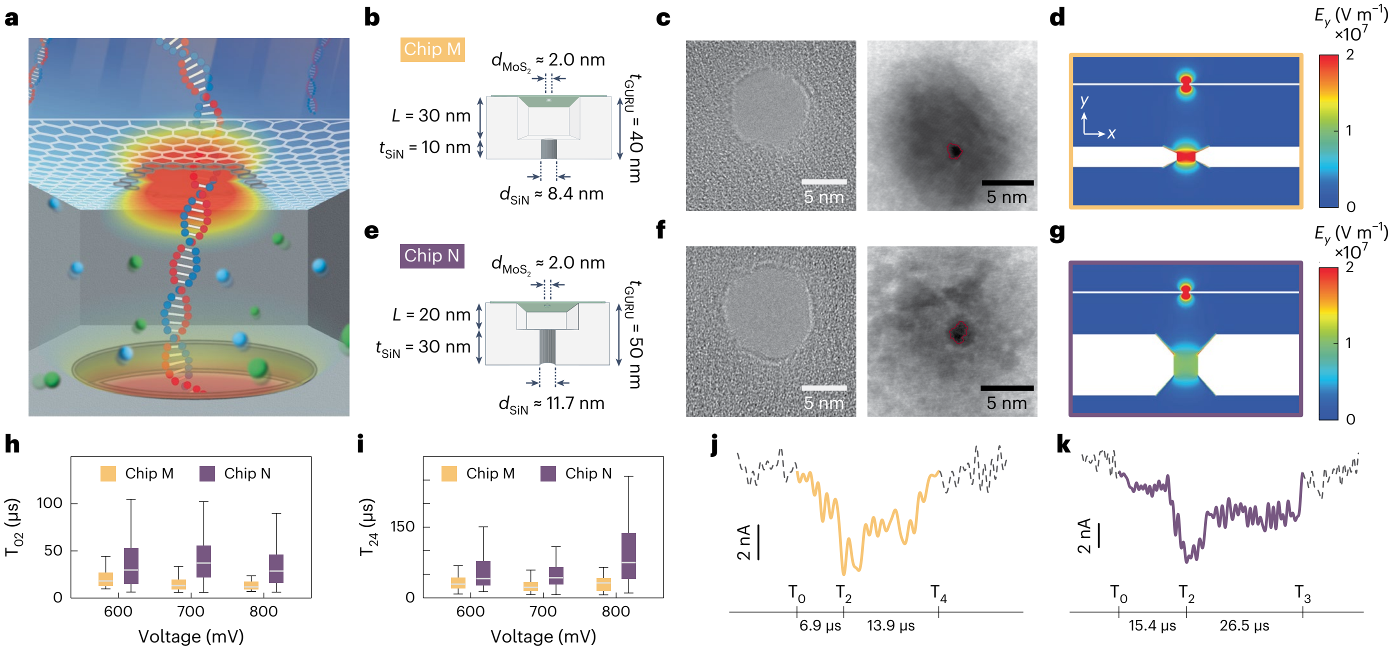

Fig. 5 | Tailoring device geometry in [1, 1] configuration to modulate the coupled electric field. a, Schematic illustration demonstrating the manipulation of a coupled electric field for molecule detection. **b**–**g**, Schematics (**b**,**e**), TEM images (**c**,**f**), and simulated electric field profiles (**d**,**g**) for Chips M (**b**–**d**) and N (**e**–**g**). **c**,**f**, Left: bright-field TEM image for SiN pore only. Right: dark-field AC-STEM image for 2D MoS$_2$ pore on top of the SiN trench and pore. **h**,**i**, Boxplots for sublevel event dwell times T$_{02}$ (**h**) and T$_{24}$ (**i**) at various voltages for Chips M and N. The box ranges from the first to the third interquartile, and the median is indicated by a horizontal line within the box, with whiskers extending to the minimum and maximum values of the dataset. For Chip M, n = 23, 76 and 53 for 600, 700 and 800 mV, respectively. For Chip N, n = 149, 151 and 152 for 600, 700 and 800 mV, respectively. **j**,**k**, Sample T events from Chips M (**j**) and N (**k**), at V = 800 mV for 200 bp dsDNA, 3 M KCl, 10 MHz bandwidth, Bessel filtered at 1 MHz.

the current levels T$_1$ ≈ W$_1$, T$_3$ ≈ W$_3$, whereas T$_2$ is the current peak in T events versus the current dip W$_2$ in the W events. For ssDNA, the W current levels are about one-half the magnitude of the W levels for dsDNA (Fig. 4d). We can compare measurements of 200 nt ssDNA to 200 bp dsDNA in [1, 1] devices: in contrast to 200 nt ssDNA in Fig. 4, when 200 bp dsDNA was translocated in additional two-pore devices with similar parameters (t_{GURU} = 40 and 50 nm) shown in Fig. 5, T events dominated, indicating the causality between persistent lengths and event shapes between ssDNA and dsDNA.

By tailoring the pore sizes and separations, one can manipulate the coupled electric fields (Fig. 5a). We show here by changing device dimensions in the same two-pore geometry, how to locally weaken the vertical component of the electric field, E_y, in the GURU layer and increase the overall dwell time. Figure 5 shows results from two more [1, 1] devices, Chips M (Fig. 5b,c) and N (Fig. 5e,f), with t_{SiN} = 10 ± 1 and 30 ± 1 nm, d_{SiN} (TEM) = 11.7 ± 0.6 and 8.4 ± 0.3 nm, L = 30 ± 1 and 20 ± 1 nm, while fixing the 2D MoS$_2$ nanopore diameter. This design allowed us to use the GURU layer as a 'speed bump' right before DNA enters the 2D pore. Simulated electric field profiles at 800 mV and 3 M KCl are shown in Fig. 5d,g. As fabricated, the corresponding values of E_y in 2D pores have similar values within our fabrication tolerances, −2.53 and −2.47 (×10^8 V m^{-1}), while in SiN pores, they differ by a factor of ~2 (−1.25 and −0.68 (×10^7 V m^{-1})). The hourglass SiN nanopore geometry[20,33] was used in modelling. Translocation measurements were conducted with 200 bp dsDNA in 3 M KCl at various voltages to observe T-like events, in contrast to W-like events in 200 nt ssDNA measurements shown in Fig. 4c. The high SNR allowed 10 MHz bandwidth measurements.

To probe the DNA translocation dynamics, we analysed the dwell times before and after dsDNA entered the 2D MoS$_2$ layer. The contour length of 200 bp dsDNA was longer than t_{GURU} for both devices, and T events dominated the event populations. With a weaker E_y in the SiN layer, Chip N exhibited significantly longer dwell times, T$_{02}$, T$_{24}$ and T$_{04}$, at fixed voltages than Chip M (Fig. 5h,i and Supplementary Table 2); T$_{02}$ (= T$_2$ − T$_0$) is the time interval when dsDNA travels the length of the GURU layer, and T$_{24}$ (= T$_4$ − T$_2$) is the time interval when dsDNA enters the 2D layer until it fully exits (Fig. 3c). As expected, T$_{24}$ was also consistently larger than T$_{02}$ across all devices we measured.

Conclusions

In this work, the detection of dsDNA position and travel time with two closeby nanopores ([1, 1] configuration) was experimentally possible by advancements in (1) temporal resolution (1 μs or better), permitting short feature identification, and (2) exquisite nanofabrication, permitting in-series assembly of atomically thin pores with high signal-to-noise ratios. Provided reported translocating velocity[9], dsDNA would travel L = 20 nm between layers in ~7–70 μs. Our platform, featuring an exceptional time resolution of 100 ns to 1 μs (refs. 34,35), made it feasible to capture shorter signal features, and we demonstrated such a possibility to track unmodified DNA travel across a ~20 nm distance. This capability represents an improvement of more than one order of magnitude in the smaller distance and translocation time between tracking markers shown previously for labelled dsDNA[9].

Looking forward, coupled nanopores represent a broad new concept opening possibilities in molecule transport and readout within a vast parameter space without labels or enzymes (Supplementary Section 11 and Supplementary Fig. 17). Rather than modifying molecules, nanofabrication and electronics capabilities are exploited to imprint and vary nanostructures enabling electromechanical control and detection. By constraining possible trajectories, GURU platforms guide molecules into the 2D sensing pore. Due to the coupling effect, the event shape is sensitive to fragment length of molecules and tracks their position during translocation. The flexible design of the GURU layer allows us to modulate and slow down molecules, compared with single 2D nanopores. Additional findings from modelling, including biphasic events for small d_{SiN} and high polymer charges, could be pursued in the future. Possible limitations of the GURU devices may include wetting and durability issues; however, these could be addressed with a wide range of available surface treatments and nanotechnology solutions. In the future, the GURU layer design can also accommodate different 2D materials, possibly lipid bilayer membranes and protein pores. Their reusability and scalability can further enable their potential cost efficiency. Beyond two layers, 2D multilayers may be also incorporated while improving SNR and temporal resolution[35]. Together with passive-electromechanical control shown here where voltages are fixed, GURU platforms could be augmented in the near term with active multi-channel voltage control beyond two-terminal measurements.

Online content

Any methods, additional references, Nature Portfolio reporting summaries, source data, extended data, supplementary information, acknowledgements, peer review information; details of author contributions and competing interests; and statements of data and code availability are available at https://doi.org/10.1038/s41565-024-01746-7.

References

1. Xue, L. et al. Solid-state nanopore sensors. *Nat. Rev. Mater.* **5**, 931–951 (2020).
2. Manrao, E. A. et al. Reading DNA at single-nucleotide resolution with a mutant MspA nanopore and phi29 DNA polymerase. *Nat. Biotechnol.* **30**, 349–353 (2012).
3. Danda, G. & Drndić, M. Two-dimensional nanopores and nanoporous membranes for ion and molecule transport. *Curr. Opin. Biotechnol.* **55**, 124–133 (2019).
4. Healy, K., Schiedt, B., Morrison, I. P. & Morrison, A. P. Solid-state nanopore technologies for nanopore-based DNA analysis. *Nanomedicine* **2**, 875–897 (2007).
5. Branton, D. et al. The potential and challenges of nanopore sequencing. *Nat. Biotechnol.* **26**, 1146–1153 (2008).
6. Dekker, C. Solid-state nanopores. *Nat. Nanotechnol.* **2**, 209–215 (2007).
7. Deamer, D. W. & Akeson, M. Nanopores and nucleic acids: prospects for ultrarapid sequencing. *Trends Biotechnol.* **18**, 147–151 (2000).
8. Chen, K., Gularek, F., Liu, B., Weinhold, E. & Keyser, U. F. Electrical DNA sequence mapping using oligodeoxynucleotide labels and nanopores. *ACS Nano* **15**, 2679–2685 (2021).
9. Chen, K. et al. Dynamics of driven polymer transport through a nanopore. *Nat. Phys.* **17**, 1043–1049 (2021).
10. Niedzwiecki, D. J. et al. Devices for nanoscale guiding of DNA through a 2D nanopore. *ACS Sens.* **6**, 2534–2545 (2021).
11. Cadinu, P. et al. Double barrel nanopores as a new tool for controlling single-molecule transport. *Nano Lett.* **18**, 2738–2745 (2018).
12. Rand, A. et al. Electronic mapping of a bacterial genome with dual solid-state nanopores and active single-molecule control. *ACS Nano* **16**, 5258–5273 (2022).
13. Pud, S. et al. Mechanical trapping of DNA in a double-nanopore system. *Nano Lett.* **16**, 8021–8028 (2016).
14. Chou, Y.-C., Chen, J., Lin, C.-Y. & Drndić, M. Engineering adjustable two-pore devices for parallel ion transport and DNA translocations. *J. Chem. Phys.* **154**, 105102 (2021).
15. Pedone, D., Langecker, M., Abstreiter, G. & Rant, U. A pore–cavity–pore device to trap and investigate single nanoparticles and DNA molecules in a femtoliter compartment: confined diffusion and narrow escape. *Nano Lett.* **11**, 1561–1567 (2011).
16. Langecker, M., Pedone, D., Simmel, F. C. & Rant, U. Electrophoretic time-of-flight measurements of single DNA molecules with two stacked nanopores. *Nano Lett.* **11**, 5002–5007 (2011).
17. Liu, X., Skanata, M. M. & Stein, D. Entropic cages for trapping DNA near a nanopore. *Nat. Commun.* **6**, 6222 (2015).
18. Merchant, C. A. et al. DNA translocation through graphene nanopores. *Nano Lett.* **10**, 2915–2921 (2010).
19. Masih Das, P. et al. Atomic-scale patterning in two-dimensional van der Waals superlattices. *Nanotechnology* **31**, 105302 (2019).
20. Rodríguez-Manzo, J. A., Puster, M., Nicolaï, A., Meunier, V. & Drndić, M. DNA translocation in nanometer thick silicon nanopores. *ACS Nano* **9**, 6555–6564 (2015).
21. Chien, C.-C., Shekar, S., Niedzwiecki, D. J., Shepard, K. L. & Drndić, M. Single-stranded DNA translocation recordings through solid-state nanopores on glass chips at 10 MHz measurement bandwidth. *ACS Nano* **13**, 10545–10554 (2019).
22. Fischbein, M. D. & Drndić, M. Electron beam nanosculpting of suspended graphene sheets. *Appl. Phys. Lett.* **93**, 113107 (2008).
23. Thiruraman, J. P., Masih Das, P. & Drndić, M. Stochastic ionic transport in single atomic zero-dimensional pores. *ACS Nano* **14**, 11831–11845 (2020).
24. Masih Das, P. et al. Controlled sculpture of black phosphorus nanoribbons. *ACS Nano* **10**, 5687–5695 (2016).
25. Briggs, K. et al. DNA translocations through nanopores under nanoscale preconfinement. *Nano Lett.* **18**, 660–668 (2018).
26. Alibakhshi, M. A. et al. Scaled-up synthesis of freestanding molybdenum disulfide membranes for nanopore sensing. *Adv. Mater.* **35**, 2207089 (2023).
27. Lin, C.-Y. et al. Modulation of charge density and charge polarity of nanopore wall by salt gradient and voltage. *ACS Nano* **13**, 9868–9879 (2019).
28. Wanunu, M. et al. Rapid electronic detection of probe-specific microRNAs using thin nanopore sensors. *Nat. Nanotechnol.* **5**, 807–814 (2010).
29. Kowalczyk, S. W., Tuijtel, M. W., Donkers, S. P. & Dekker, C. Unraveling single-stranded DNA in a solid-state nanopore. *Nano Lett.* **10**, 1414–1420 (2010).
30. Brinkers, S., Dietrich, H. R. C., De Groote, F. H., Young, I. T. & Rieger, B. The persistence length of double stranded DNA determined using dark field tethered particle motion. *J. Chem. Phys.* **130**, 215105 (2009).
31. Bell, N. A. W., Chen, K., Ghosal, S., Ricci, M. & Keyser, U. F. Asymmetric dynamics of DNA entering and exiting a strongly confining nanopore. *Nat. Commun.* **8**, 380 (2017).
32. Carson, S., Wilson, J., Aksimentiev, A. & Wanunu, M. Smooth DNA transport through a narrowed pore geometry. *Biophys. J.* **107**, 2381–2393 (2014).
33. Chou, Y.-C., Masih Das, P., Monos, D. S. & Drndić, M. Lifetime and stability of silicon nitride nanopores and nanopore arrays for ionic measurements. *ACS Nano* **14**, 6715–6728 (2020).
34. Shekar, S. et al. Measurement of DNA translocation dynamics in a solid-state nanopore at 100 ns temporal resolution. *Nano Lett.* **16**, 4483–4489 (2016).
35. Lin, C.-Y. et al. Ultrafast polymer dynamics through a nanopore. *Nano Lett.* **22**, 8719–8727 (2022).

Methods

GURU fabrication in SiN layer

To fabricate the trench region within the GURU devices, the 5 mm chips are first made through traditional microfabrication methods[28,36] to create a suspended SiN membrane window, from bottom to top, a 500 µm silicon substrate, a 5 µm thermal SiO_2 and a 40 nm (or 120 nm) low-stress low pressure chemical vapor deposition SiN. The chip is first spin-coated with C4 poly(methyl methacrylate) at 4,000 rpm for 60 s, followed by a 10 min baking at 180 °C. A pair of two-square patterns, 400 by 400 nm^2, is exposed onto the resist layer (Elionix ELS-7500EX). The resist is developed in 1:3 v/v methyl isobutyl ketone:isopropyl alcohol (IPA) solution for 60 s and rinsed in IPA for 2 min. Combining RIE with trifluoromethane and oxygen (CHF_3/O_2) at a rate of ~1 nm s^{-1}, we can remove SiN within the patterned area[28,36] to the desired trench depth, L. Before fabricating nanopores in the SiN layer, boiling piranha solution (1:3 v/v H_2O_2:H_2SO_4) is used for 10–15 min to remove the leftover resist and any organic contamination.

We used two methods to fabricate nanopores in the SiN layer: TEM drilling and a combination of EBL and RIE (Extended Data Fig. 1). The combination of EBL and RIE is the preferred choice for producing nanopore arrays in the SiN layer, primarily due to their efficiency in speed and scalability compared with TEM drilling. The precision of RIE anisotropic etching of SiN allows only selected areas to have pores (Chips D and J). For some devices, assisted with TEM, we bypassed EBL limitations to fabricate smaller nanopores (Chip E). TEM drilling is convenient for making [1, 1] devices (Chips L, M and N) and [N, 1] devices with a small number and smaller diameter of SiN pores (Chips A, B and C). For in situ room temperature TEM drilling, we operate at 200 kV for high-resolution TEM mode (JEOL F200). This operating mode allows us to locate the thinned square region and fabricate one nanopore at a time to desired numbers[14]. On the other hand, to quickly fabricate a large number of nanopores onto the SiN layer, 1:2 dilution of ZEP520A:anisole is spin-coated at 4,000 rpm for 40 s, followed by 2 min baking at 180 °C. Array patterning is exposed onto the resist layer (Elionix ELS-7500EX) with a shot pitch of 150 nm (ref. 33). The resist is then developed in *o*-xylene for 70 s and IPA for 30 s. Controlling the etching time in RIE, we can fabricate nanopores only in the previously thinned square area, instead of creating a nanoporous SiN membrane. The resist is then stripped off by placing the membrane in heated *N*-methyl-2-pyrrolidone at 60 °C for 3 h and then rinsed with IPA. Before transferring 2D layers onto the device, another round of 10 min piranha cleaning is performed.

2D MoS_2 growth, device integration and nanopore drilling

Monolayer MoS_2 flakes were grown via chemical vapour deposition (schematic shown in Supplementary Fig. 18) following a previously described process[37]. Solutions of ammonium heptamolybdate tetrahydrate (9 mM) and sodium cholate (23 mM) in deionized (DI) water were spin-coated onto a piranha-cleaned Si/SiO_2 substrate (300 nm SiO_2). The substrate was placed in a 1 inch tubular furnace (Thermo Scientific Lindberg/Blue M), and 150 mg of sulfur was placed on a second SiO_2/Si substrate 22 cm upstream. The furnace was flushed with N_2 gas flow (1,000 sccm) for 10 min, after which the growth substrate was heated at a rate of 70 °C min^{-1} and kept at 750 °C for 15 min under 400 sccm N_2 gas flow. During growth, the sulfur was kept at a temperature of 180 °C. After growth, the samples were rapidly cooled by turning off and opening the furnace.

After the SiN scaffold fabrication process and piranha cleaning, monolayer MoS_2 flakes were transferred onto the GURU devices following a wet transfer process[38]. After chemical vapour deposition growth, a piece of SiO_2/Si substrate coated with MoS_2 flakes was spin-coated with PMMA and placed on a 1 M KOH solution to etch the underlying SiO_2. The floating PMMA film with MoS_2 flakes was then washed by transferring it to a large volume of DI water before being scooped up and transferred onto the device and positioned under an optical microscope so that a single monolayer MoS_2 flake fully covered the patterned window (Extended Data Fig. 5). After drying for 1 h in the air, the PMMA was removed with acetone and subsequent rapid thermal annealing in Ar:H_2 mixture.

Two-dimensional MoS_2 imaging and nanopore drilling were performed on a Cs-corrected JEOL NEOARM scanning transmission electron microscope operating at 80 kV. The nanopores were drilled by scanning the electron probe over a selected area ranging from 1 to 9 nm^2 for up to 10 s. With this technique, we can create nanopores with tailored sizes in a controlled manner.

Device wetting and storage procedure

The wetting procedure was developed in this work. It begins with mixing equal amount of EtOH:H_2O (v/v = 1/1) solutions (HPLC grade ethanol from Fisher Chemical and DI water) at room temperature. This wetting solution is then undergoing vacuum degassing for 30 min. Right after drilling the nanopore in the 2D layer, the GURU device is immersed in the degassed solution for 30–60 min.

Determining nanopore geometries and error estimation in thickness

The GURU membrane thickness, t_{SiN}, is measured by ellipsometry after fabrication. The initial pore diameters, d, are measured from TEM images, corresponding to the smallest constriction region within the pore, error is determined as discussed in Supplementary Fig. 19. We note the limitation of TEM diameters as pores could change over time and measurements[33]. The interlayer separation, L, is calibrated by RIE etching time (etching rate ~1 nm s^{-1}) and the starting membrane thickness. We estimate the error in L to originate from fluctuations in the starting deposition thickness (~40 nm) and the error in etching time (~1 s) performed by the user. This translates to an estimated error in L. Based on this, we quote in the main text $L = 20 \pm 1$ nm and $t_{GURU} = 40 \pm 3$ nm.

Ionic measurements and DNA sample

The recording bandwidth of a 1 MHz VC100 amplifier (Chimera Instruments)[14] and that of a 10 MHz amplifier (Elements SRL)[35] were utilized to read ionic signals by applying an external bias voltage via a two-terminal set of Ag/AgCl electrodes (Supplementary Fig. 20 for noise performance). Two types of nanopore flow cell were used in this work to host the GURU devices. Conventional one-piece PDMS flow cells[39] are used for devices measured in Fig. 2, where the devices are glued to the flow cell with silicone elastomers (Supplementary Fig. 21a). The other customized two-part PMMA flow cell[35] (Supplementary Fig. 21b) was used to house the device measured in Fig. 4. Within this design, two complementary PMMA parts are manufactured with a cavity for the GURU device, and fluidic channels connect reservoirs with a volume between 60 and 70 µl. To assemble and secure the GURU device, the device is sandwiched between two silicon gaskets, labelled as O-rings, which are subsequently compressed by the PMMA plastic parts. Some examples of current traces are given in Supplementary Fig. 22. We note that the applied voltage and the concentration of salt solutions in this dataset were limited not by the device but by the amplifier current limit. Results in this paper are based on translocation data from three devices with a configuration [N, 1] and three devices with a configuration [1, 1].

The DNA samples used for ionic measurements were 1,500 bp dsDNA (200 nM, NoLimits, ThermoFisher Scientific; Fig. 4b), 200 bp dsDNA (20 nM; Fig. 5) and 90 nt ssDNA (200 nM; Fig. 2d,e) and 200 nt ssDNA (200 nM, IDT; Fig. 4b) and authenticated by the company. Samples were prepared in TE buffer (10 mM Tris and 1 mM EDTA) and 1 M and 3 M KCl electrolyte solution (pH 8.0) at room temperature. The oligo sequence for 90 nt ssDNA is GCGTAATACGACTCACTATAGTCTTTGCAGCACCGACACCTGAACTTCCACCCTTCTTTCAAGTCATGTTCTTAGTGAGGGTTAATTCG and for 200 nt ssDNA is GCGTAATACGACTCACTATAGTCTTTGCAGCACCGACAC-

CTGAACTTCCACCCTTCTTTCAAGTCATGTTCTTTAGTGAGGGTTAATTCGCCCCCCCCCCCCCCCCCCCCCGCGTAATACGACTCACTATAGTCTTTGCAGCACCGACACCTGAACTTCCACCCTTCTTTCAGTCATGTTCTTTAGTGAGGGTTAATTCG.

The 2D pore diameters were less than the cross-sectional size of doubly folded dsDNA to avoid or minimize multistep events due to dsDNA folding. We rely on event statistics combined with modelling to interpret the dominant and characteristic translocation signals as dsDNA tracking rather than due to dsDNA folding (Figs. 4 and 5).

Data analysis details

Event identification and characterization such as in Fig. 4 and Supplementary Fig. 23 are completed in a two-step process. Baseline correction and threshold detection[35] is first used to extract events from filtered current traces (Supplementary Fig. 24). Event types and features are then inspected manually for subsequent analysis. We note that the typical characterization used in the solid-state nanopore field defining the mean event depths and durations is not particularly meaningful and informative for data containing characteristic T-like and W-like event patterns. For event analysis in Figs. 4 and 5, we consider events longer than 10 µs (or 1 µs), corresponding to the digital Bessel filter we applied to the cut-off frequency, 100 kHz (or 1 MHz). Event characterization tools and an interactive graphical user interface for feature selection can be found at https://github.com/joshualchen/Clampfit.

Device statistics and reproducibility

We inspected each device with optical microscopy to preliminarily confirm whether the 2D flakes and SiN membrane were still intact. Over 36 devices were fabricated to test the feasibility of the manufacturing steps and to test DNA translocations. Most devices were designed to have 1–2 nm diameter 2D pores on high-quality monolayer MoS_2 flakes. However, in a few cases, accidental overexposure to the electron beam resulted in larger-than-desired 2–3 nm diameter pores. About 13% of the devices experienced wetting issues and we were not able to record reliable data. Some devices initially showed stable ionic currents but later overloaded the amplifier owing to fluid cell leaks, broken 2D flakes or nanopore expansions. More details of observed issues can be found in Supplementary Section 19. We did not perform a statistical study of all outcomes and yields, yet focused on obtaining a sufficient number of conducting and high-quality chips, which was accomplished in this study.

Data availability

Source data and analysis codes are available via the figshare repository at https://doi.org/10.6084/m9.figshare.26132701. Other details are also available upon request for purposes of reproducing or extending the work and analysis. If devices are requested such as 2D materials or GURU devices, this may be possible as well if resources for device nanomanufacturing are available.

References

36. Venta, K. et al. Differentiation of short, single-stranded DNA homopolymers in solid-state nanopores. *ACS Nano* **7**, 4629–4636 (2013).
37. Parkin, W. M. et al. Raman shifts in electron-irradiated monolayer MoS_2. *ACS Nano* **10**, 4134–4142 (2016).
38. Mlack, J. T. et al. Transfer of monolayer TMD WS2 and Raman study of substrate effects. *Sci. Rep.* **7**, 43037 (2017).
39. Balan, A. et al. Improving signal-to-noise performance for DNA translocation in solid-state nanopores at MHz bandwidths. *Nano Lett.* **14**, 7215–7220 (2014).

Acknowledgements

We acknowledge use of the JEOL F200 TEM and JEOL NEOARM in the NSF-MRSEC electron microscopy facility at the University of Pennsylvania. The work was performed in the David Rittenhouse Laboratory and at the Singh Center for Nanotechnology, an NNCI member supported by NSF grant no. ECCS-15421153. This work was partially funded by NSF grants 2002477 and 1905045, NIH grant R21 HG0101536 and CHOP institutional funds.

Author contributions

Y.-C.C. and C.-Y.L. contributed equally to the work. Y.-C.C., D.M. and M.D. conceptualized and conceived the project. Y.-C.C., C.-Y.L., A.C., R.K. and P.Y. fabricated GURU devices and nanopores. Y.-C.C. and A.C. prepared DNA samples. Y.-C.C., C.-Y.L. and A.C. performed the ionic measurements. Y.-C.C. and C.-Y.L. performed gel electrophoresis and analysis. Y.-C.C., C.-Y.L., J.C. and A.C. performed data analysis. Y.-C.C., C.-Y.L., J.C., A.C., D.M. and M.D. constructed and approved the manuscripts. D.M. and M.D. supervised the project.

Competing interests

The authors declare no competing interests.

Additional information

Extended data is available for this paper at https://doi.org/10.1038/s41565-024-01746-7.

Supplementary information The online version contains supplementary material available at https://doi.org/10.1038/s41565-024-01746-7.

Correspondence and requests for materials should be addressed to Marija Drndić.

Peer review information *Nature Nanotechnology* thanks the anonymous reviewers for their contribution to the peer review of this work.

Reprints and permissions information is available at www.nature.com/reprints.

https://doi.org/10.1038/s41565-024-01746-7

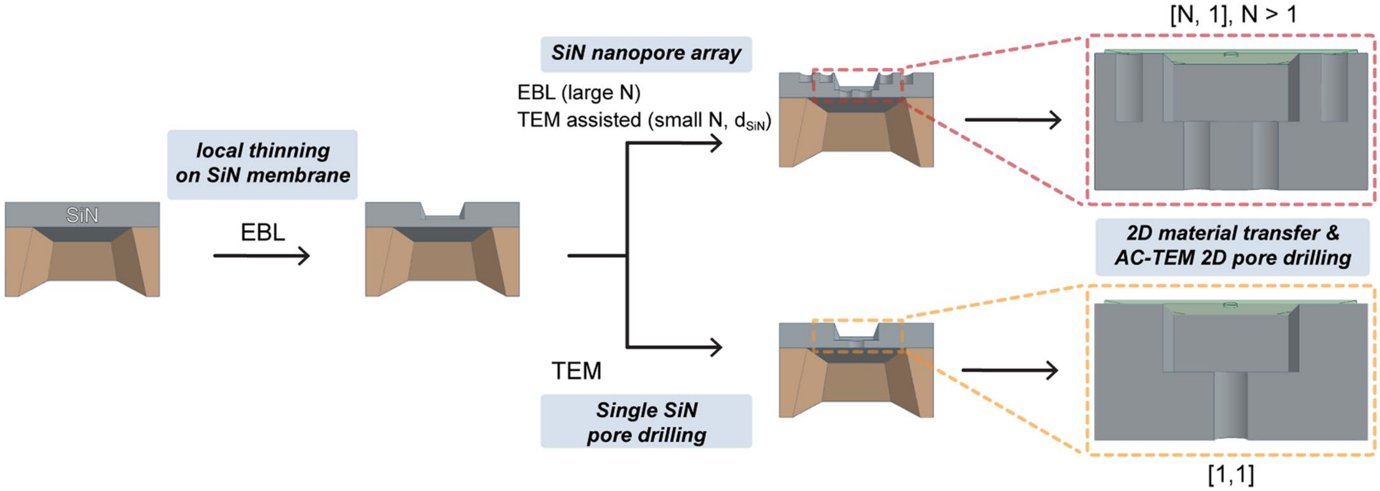

Extended Data Fig. 1 | Schematic illustration of the fabrication process for the 2D-GURU devices with different configurations. There are two complementary ways to make the pores in the underlying SiN layer. Electron beam lithography (EBL) is typically used to create nanopore arrays in the SiN layer, forming an [*N*, 1] configuration. The second way to make SiN pores is with transmission electron microscopy (TEM) drilling. Using TEM sculpting to drill a single pore in the SiN layer results in a device with a [1, 1] configuration. Some [*N*,1] devices with small *N* and small SiN pore diameter, d_{SiN} (~10 nm or less in diameter) were also made with TEM sculpting (Fig. 2a in the main paper). After fabricating SiN pores in the trench region, we deposit the 2D material flake onto the trench, followed by AC-STEM drilling of the 2D pore. Supplementary Table 1 provides an index of TEM images for GURU devices with various configurations.

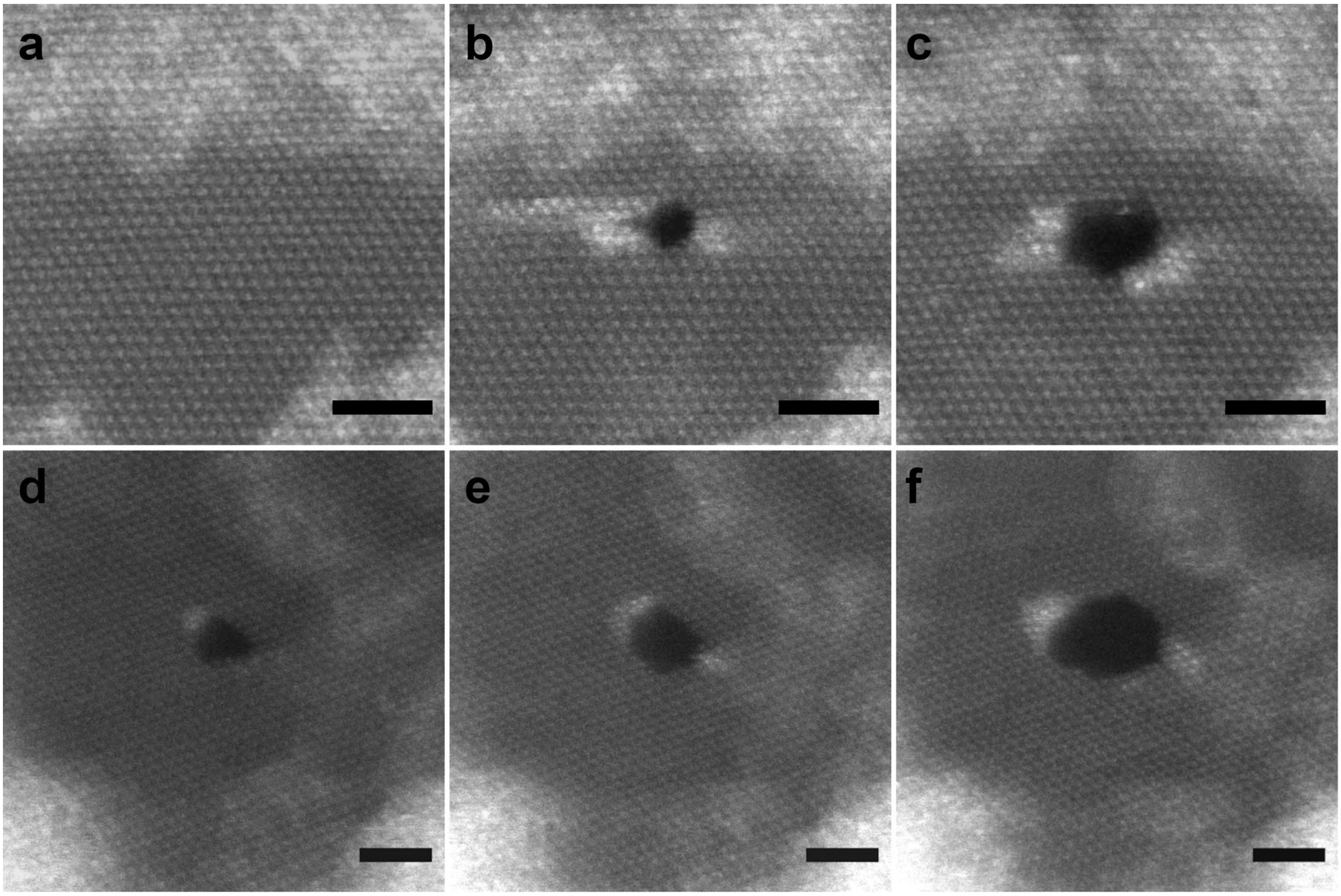

Extended Data Fig. 2 | Nanopore size control throughout the AC-STEM drilling process. Series of ADF-STEM (annular dark field scanning transmission electron microscopy) images of suspended monolayer MoS_2 during the nanopore drilling process on two different devices. Some accumulation of atoms on the pore edges is visible and this can contribute to an increased effective thickness of the pore in some cases. **(a)** MoS_2 lattice before drilling, **(b)** after a few seconds of drilling, a sub-nanometer pore is created (size ~ 0.85 nm x 0.85 nm), **(c)** same nanopore after a few additional seconds of drilling, yielding a final nanopore with a size adapted to ssDNA translocation measurements (~ 1.7 nm x 1.3 nm). This pore is a part of a [6,1] device configuration. **(d-f)** Images of the same process on another GURU device, aiming for a nanopore size adapted to translocation measurements of dsDNA. Pore sizes are ~ 1.29 nm x 1.47 nm, 1.81 nm x 1.89 nm, 2.17 nm x 3.15 nm for D, E and F, respectively. These sizes are extracted from two intensity profiles taken at the widest points of the pore vertically and horizontally, respectively. All scale bars are 2 nm.

https://doi.org/10.1038/s41565-024-01746-7

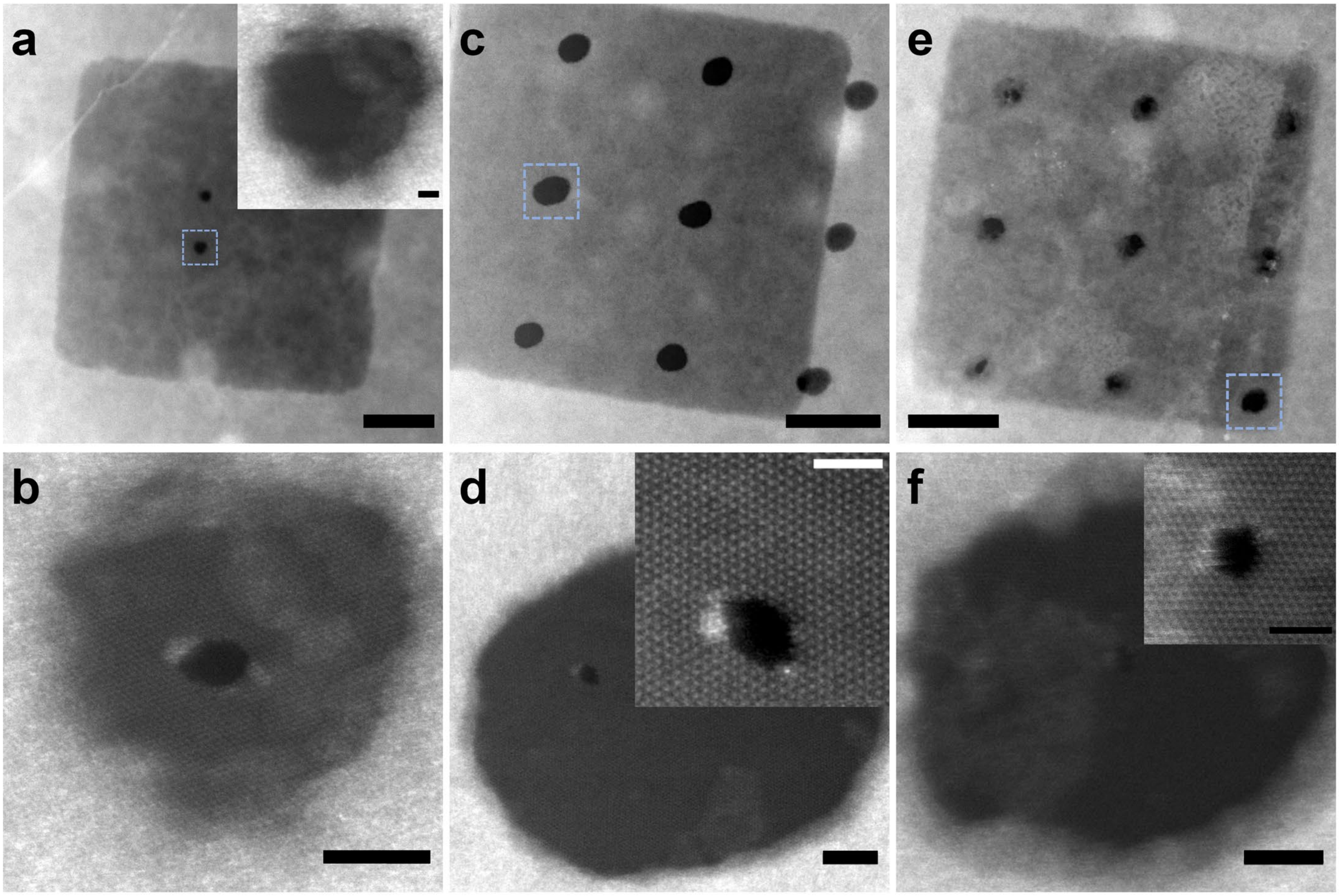

Extended Data Fig. 3 | Additional examples of 2D MoS_2 nanopore drilling for three other GURU devices with varying geometries. (a, b) [2,1], (c, d) [6,1], (e, f) [9,1]. ADF-STEM (annular dark field scanning transmission electron microscope) images of **(a)** RIE-thinned region of the SiN membrane containing two TEM-drilled nanopores (inset: closeup of the bottom nanopore covered by monolayer MoS_2 prior to drilling; **(b)** 2D nanopore above the SiN pore; **(c)** pre-patterned RIE-thinned square in the SiN membrane containing six EBL-made nanopores, **(d)** closeup of pore highlighted by the blue dashed square in (c), showing the suspended monolayer MoS_2 after AC-STEM drilling (inset: high resolution image of the 2D nanopore), **(e)** pre-patterned RIE-thinned square in the SiN membrane containing nine EBL-made nanopores, **(f)** closeup of pore highlighted by the blue dashed square in (e) showing the suspended monolayer MoS_2 after AC-STEM drilling (inset: high resolution image of the 2D nanopore). (e) and (f) are images of the reused device shown in Fig. 2a in the main text, the STEM drilling step shown here corresponds to the fourth MoS_2 transfer process, and third STEM drilling that this device underwent. Scale bars are 100 nm for (a), (b) and (c), 5 nm for (d), (e) and (f), and 2 nm in all inset images.

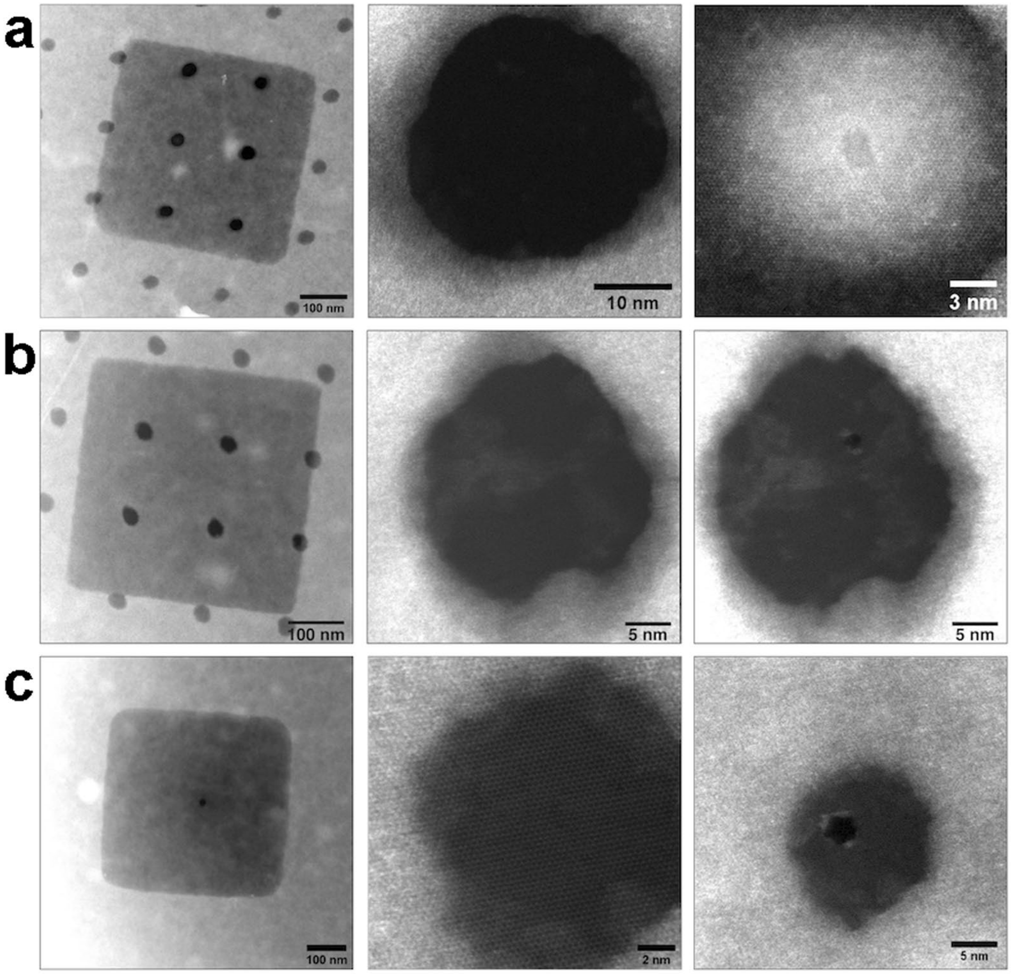

Extended Data Fig. 4 | Additional images of 2D-GURU devices. (a) [6,1] from Fig. 2b (Chip J); **(b)** [4,1] from Supplementary Fig. 3 (Chip K); **(c)** [1,1] from Fig. 4, before and after 2D pore formation (Chip L).

https://doi.org/10.1038/s41565-024-01746-7

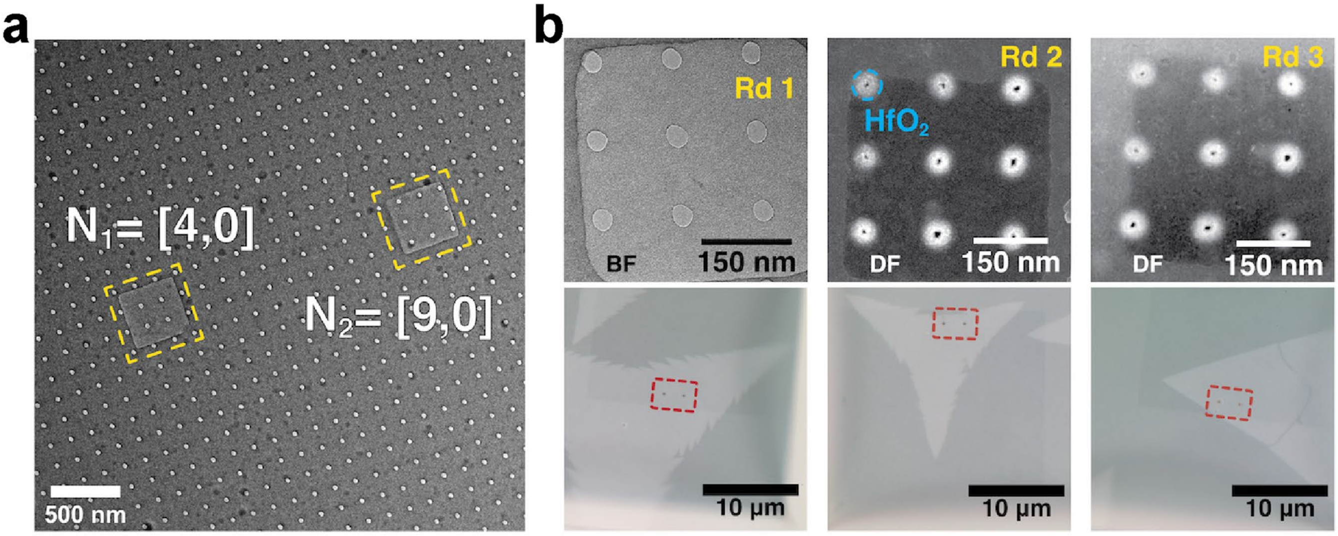

Extended Data Fig. 5 | Reusability and Versatility of 2D-GURU Devices. **(a)** TEM images showing two patterned windows on top of which 2D material is deposited. The 2D pores can be selectively drilled in multiple desired locations. **(b)** Series of TEM images (top) and optical images (bottom) after the same device was reused. On this device we deposited ALD (atomic layer deposition) HfO_2 (~ 3 nm) after the first round of measurement, which can be seen as the white circles around the pore edges. The position of two patterned windows is highlighted in dotted red squares. Devices presented in the main text do not contain the HfO_2 layer and this device in Extended Data Fig. 5b was used for wetting and ionic measurement tests.

Extended Data Table 1 | Comparison of two-pore devices

type of material	d_1 (nm) [a]	d_2 (nm) [a]	L [b]	molecule	ref
SiN / Si	30	700	~2.3 μm	λ DNA, nanoparticles [c]	15
SiN / Si	28	23	1.5 μm	dsDNA	16
SiN / SiN	~10	> 230	> 2 μm	λ DNA	17
MoS_2 / SiN	2	~ 10	20 nm	dsDNA, ssDNA	this work

[a] diameter, [b] interlayer separation.

[c] For nanoparticle detection experiments, pore diameters were 50 nm (SiN) and 150 nm (Si).